Smoothed particle hydrodynamics in a generalized coordinate system with a finite-deformation constitutive model

Yashiro, Shigeki
Department of Mechanical Engineering, Shizuoka University

Okabe, Tomonaga
Department of Aerospace Engineering, Tohoku University

https://hdl.handle.net/2324/4476056

出版情報：International Journal for Numerical Methods in Engineering. 103 (11), pp.781-797, 2015-04-16. John Wiley and Sons
バージョン：
権利関係：

International Journal for Numerical Methods in Engineering 2015; 103:781–797
DOI: 10.1002/nme.4906

Smoothed particle hydrodynamics in a generalized coordinate system with a finite-deformation constitutive model

Shigeki Yashiro [a,*], Tomonaga Okabe [b]

[a] Department of Mechanical Engineering, Shizuoka University

3-5-1 Johoku, Naka-ku, Hamamatsu 432-8561, Japan

[b] Department of Aerospace Engineering, Tohoku University

6-6-01, Aoba-yama, Aoba-ku, Sendai 980-8579, Japan

* Corresponding author: Tel: +81-53-478-1026; Fax: +81-53-478-1026.

E-mail address: yashiro.shigeki@shizuoka.ac.jp (S. Yashiro)

Abstract

This study proposes smoothed particle hydrodynamics (SPH) in a generalized coordinate system. The present approach allocates particles inhomogeneously in the Cartesian coordinate system, and arranges them via mapping in a generalized coordinate system in which the particles are aligned at a uniform spacing. This characteristic enables us to employ fine division only in the direction required, e.g., in the through-thickness direction for a thin-plate problem, and thus to reduce computation cost. This study provides the formulation of SPH in a generalized coordinate system with a finite-deformation constitutive model and then verifies it by analyzing quasi-static and dynamic problems of solids. High-velocity impact test was also performed with an aluminum target and a steel sphere, and the predicted crater shape agreed well with the experiment. Furthermore, the numerical study demonstrated that the present approach successfully reduced the computation cost with marginal degradation of accuracy.

Keywords: Solids, Particle methods, Impact, Mapping

1. Introduction

Meshless methods will overcome difficulties associated with reliance on a mesh to construct the approximation when analyzing moving discontinuities. One of the first meshless methods is smooth particle hydrodynamics (SPH) developed by Gingold and Monaghan [1] and Lucy [2]. Another most popular meshless methods are the element-free Galerkin (EFG) method [3], the reproducing kernel particle method (RKPM) [4], and the meshless local Petrov-Galerkin (MLPG) method [5]. A number of different meshless methods [6-12] have been developed in recent years, and a good review on meshless methods and their implementation can be found in literature, e.g., [13].

Among them, SPH has been improved and been applied to engineering problems by many researchers. This method was first developed to predict astrophysical phenomena with compressible flow [1,2], and has been applied to incompressible flow [14], viscous flow [15-18], and solids [19-23]. A coupled analysis between fluid and structure has also been performed [24,25]. In recent years, SPH has been used in a wide range of engineering fields including high- and hyper-velocity impact in armor systems [26] and space debris shields [27,28], machining [29], die casting and forging of metals [30,31], dam spillway flow [32], and geophysical problems of magma chambers [33] and lava flow [34]. Recent reviews of SPH can be found in the literature [35,36].

In standard SPH, particles initially have to be aligned at uniform intervals in the Cartesian coordinate system. Specifically, when analyzing thin-plate problems, fine division is necessary in the through-thickness direction to achieve sufficient accuracy. However, close particle spacing drastically increases the calculation cost due to the increase in the total number of particles. The particle spacing can be altered in part of an analytical model (but still be uniform)

[24,28]. This method will be useful in problems where stresses change steeply only in a limited region of the model. However, fine particles must be used over the whole model if a steep stress gradient is possible throughout the model.

In recent years, a number of researchers have investigated accuracy improvement of SPH. Wong and Shie [37] developed a Galerkin-based SPH formulation with moving least-squares approximation in combination with updated Lagrangian kernel functions to remove instabilities. They applied it to impact problems with large deformation. Herreros and Mabssout [38] proposed Taylor-SPH with a two-step time-discretization scheme and demonstrated its accuracy by predicting shock-wave propagation. Blanc and Pastor [39] extended the algorithm using a Runge-Kutta integration scheme to improve the accuracy and stability for large deformation problems. Colagrossi et al. [40] proposed a particle-packing algorithm to reduce numerical noise due to particle resettlement during the early stages of the flow evolution. Vacondio et al. [41] proposed a variable resolution scheme that dynamically modified particle sizes by splitting and merging individual particles to provide good resolution. Puri and Ramachandran [42] compared the accuracy and robustness between the current state-of-the-art SPH schemes, namely standard SPH with an adaptive density kernel estimation technique, the variational SPH formulation, and the Godunov-type SPH scheme, for compressible Euler equations.

However, few studies seek to reduce computation costs. Maurel and Combescure [43] introduced Mindlin-Reissner’s thick shell theory into SPH to reduce computation cost for analyzing thin structures. A thin plate is modeled by a single layer of particles having three degrees of freedom in translation and two degrees of freedom in rotation. They successfully applied it to impact fracture. Furthermore, Combescure and colleagues [44] extended the SPH shells to represent dynamic fracture with sharp discontinuities.

Fine particles will be used for analyzing extension of microscopic damage in materials such as composite laminates [45], but in some cases, fine division will be required only in the through-thickness direction. This study therefore proposes SPH in a generalized coordinate system to achieve inhomogeneous particle placement. More specifically, we allocate particles inhomogeneously in the Cartesian coordinate system, and then arrange them at a uniform interval in a generalized coordinate system via mapping. The conservation equations, as well as the updates in the particle positions, are solved in the mapped space by using the standard scheme of SPH. This enables us to obtain fine division only in the direction required, e.g., in the through-thickness direction for a thin-plate problem. This method can be a breakthrough improving the computational efficiency of SPH by reducing the total number of particles.

This paper is organized as follows. Section 2 provides the formulation of SPH in a generalized coordinate system with a finite-deformation constitutive model. In Section 3, the newly developed SPH is applied to quasi-static bending problem of a thin plate for verification. Accuracy of the bending results is compared between the present approach and the standard method to demonstrate the advantage of the use of a generalized coordinate system. Finally, Section 4 presents the experiment and analysis of high-velocity impact of a steel sphere on an aluminum plate. We will discuss validity and usefulness of SPH in a generalized coordinate system.

2. Theory

2.1 Generalized coordinate system

Consider the origin O, the regular Cartesian coordinate system (x^1, x^2, x^3), and a generalized coordinate system (θ^1, θ^2, θ^3). Coordinates θ^1, θ^2, and θ^3 are equal to coordinates x^1, x^2, and x^3 multiplied by $1/a$, $1/b$, and $1/c$. Here, a variable with a superscript (subscript) denotes a contravariant (covariant) component of a tensor. An arbitrary vector $\mathbf{R}$ is represented by

$\mathbf{R} = x^i \mathbf{e}_i = \theta^i \mathbf{g}_i$, where $\mathbf{e}_i$ and $\mathbf{g}_i$ (i = 1, 2, 3) are the orthonormal base unit vector and the covariant base vector. The covariant base vector is calculated by

$$\mathbf{g}_i = \frac{\partial \mathbf{R}}{\partial \theta^i} = \frac{\partial x^j}{\partial \theta^i} \mathbf{e}_j . \tag{1}$$

Equation (1) provides the relations of $\mathbf{g}_1 = a\mathbf{e}_1$, $\mathbf{g}_2 = b\mathbf{e}_2$, and $\mathbf{g}_3 = c\mathbf{e}_3$ for the coordinate system considered. The contravariant base vector $\mathbf{g}^i$ is given by

$$\mathbf{g}^i = \frac{\partial \theta^i}{\partial x^j} \mathbf{e}_j . \tag{2}$$

The following relations are derived between the covariant base vector and the contravariant base vector based on a generalized tensorial analysis.

$$\mathbf{g}_i \cdot \mathbf{g}_j = g_{ij} \tag{3}$$

$$\mathbf{g}^i \cdot \mathbf{g}^j = g^{ij} \tag{4}$$

$$\mathbf{g}_i \cdot \mathbf{g}^j = \delta_i^j \tag{5}$$

$$\mathbf{g}^i = g^{ij} \mathbf{g}_j \tag{6}$$

$$\mathbf{g}_i = g_{ij} \mathbf{g}^j \tag{7}$$

g_{ij} (g^{ij}) is the covariant (contravariant) metric tensor, and δ_i^j is the unit tensor. These equations transform the covariant component into the contravariant component (and vice versa) for a vector **v**.

$$v_i = g_{ih} v^h \quad \text{and} \quad v^i = g^{ih} v_h \tag{8}$$

Now, let us define parameters $\tilde{h}_i$ and g that relate the components of an arbitrary tensor in the physical space to those in the mathematical space.

$$\tilde{h}_i = \frac{1}{\sqrt{g_{ii}}} \quad \text{(no sum on } i\text{)} \tag{9}$$

$$g = \left| g_{ij} \right| = a^2 b^2 c^2 \tag{10}$$

A component of a vector $\mathbf{v} = \tilde{v}^i \mathbf{e}_i$ in the physical space is transformed into one in the considered mathematical space as follows.

$$\tilde{v}^i = \tilde{h}_i v_i \text{ and } \tilde{v}^i = \frac{v^i}{\tilde{h}_i} \text{ (no sum on } i\text{)} \tag{11}$$

This equation will be used when presenting field variables in the physical space.

2.2 Governing equations

The governing equations for continuum mechanics express the conservation of mass and momentum, and these equations are solved in the updated Lagrangian scheme. The conservation equation of mass is

$$\frac{\mathrm{d}\rho}{\mathrm{d}t} = -\rho\left[\frac{1}{\sqrt{g}}\frac{\partial\left(\sqrt{g}\,v^i\right)}{\partial\theta^i}\right], \tag{12}$$

where ρ is the density, t is the time, and v^i is the velocity. Since g is constant for the base vector in this study, Eq. (12) is simplified to

$$\frac{\mathrm{d}\rho}{\mathrm{d}t} = -\rho\frac{\partial v^i}{\partial\theta^i}. \tag{13}$$

The conservation equation of momentum is, at the current configuration,

$$\frac{\mathrm{d}v^i}{\mathrm{d}t} = \frac{1}{\rho}\sigma^{ji}\Big|_j, \tag{14}$$

where σ^{ij} is the first Piola-Kirchhoff stress tensor, and $\square|_i$ denotes the covariant derivative. Note that the Christoffel symbol is zero in the coordinate system considered, and the covariant derivative $\square|_i$ is then simplified to $\square_{,i} = \partial\square/\partial\theta^i$.

2.3 Constitutive equations

This section presents a finite-deformation constitutive model. A classical elastic-plastic theory was used, and the following rate-form potential was considered.

$$\tilde{U} = \frac{1}{2}C_{-ep}^{ijkl}D_{ij}D_{kl} \tag{15}$$

$\mathbf{C}_{-ep} = C_{-ep}^{ijkl}\mathbf{g}_i \otimes \mathbf{g}_j \otimes \mathbf{g}_k \otimes \mathbf{g}_l$ is the elastic-plastic stiffness tensor, and $\mathbf{D} = D_{ij}\mathbf{g}^i \otimes \mathbf{g}^j$ is the deformation rate tensor. Based on the von Mises plastic potential and the associated flow rule, the yield function F and basic equations are as follows.

$$F = \frac{1}{3}\left\{\bar{\sigma}^2 - \left(\sigma_y\left(\bar{e}^p\right)\right)^2\right\} \tag{16}$$

$$\bar{\sigma}^2 = \frac{3}{2}\mathbf{T}' : \mathbf{T}' \tag{17}$$

$$\mathbf{D}^p = \dot{\lambda}\mathbf{T}' \tag{18}$$

$$\dot{\lambda} = \frac{3}{2}\frac{\dot{\bar{e}}^p}{\bar{\sigma}} = \frac{\mathbf{T}' : \left(\mathbf{C}_{-e} : \mathbf{D}\right)}{\mathbf{T}' : \left(\mathbf{C}_{-e} : \mathbf{T}'\right) + \frac{4}{9}\bar{\sigma}^2 H'} \tag{19}$$

Here, $\bar{\sigma}$ is the equivalent stress, σ_y is the yield stress, $\bar{e}^p$ is the equivalent plastic strain, $\mathbf{T}'$ is the deviatoric stress tensor, and H' is the hardening coefficient. The constitutive equation is

$$\overset{\circ}{\hat{\mathbf{T}}}_t(t)_{(J)} = \mathbf{C}_{-e} : \left(\mathbf{D} - \mathbf{D}^p\right), \tag{20}$$

where the left-hand-side is the Jaumann rate of the Kirchhoff stress, $\mathbf{C}_{-e}$ is the stiffness tensor of an isotropic elastic medium, and $\mathbf{D}^p$ is the plastic strain rate. Although $\mathbf{C}_{-ep}$ in Eq. (15) can be derived, this study used Eq. (20) for stability of the analysis. The rate of the Cauchy stress is thus

$$\dot{\mathbf{T}} = \left(\mathbf{C}_{-e} : \left(\mathbf{D} - \mathbf{D}^p\right) - \dot{J}_t(t)\mathbf{T}\right) + \mathbf{W} \cdot \mathbf{T} - \mathbf{T} \cdot \mathbf{W}, \tag{21}$$

where $J_t(t)$ is the modulus of volume change, and $\mathbf{W}$ is the spin tensor.

After this point, variables in the physical space are indicated with tildes. The stiffness tensor in mathematical space, C_{-e}^{ijkl}, is converted from that in the physical space as follows.

$$C_{-e}^{ijkl} = \tilde{C}_{-e}^{ijkl}\tilde{h}_i \tilde{h}_j \tilde{h}_k \tilde{h}_l \quad \text{(no sum on } i, j, k, \text{ and } l\text{)} \tag{22}$$

When the stress tensor and strain tensor is calculated in the mathematical space, those in the physical space can be obtained by

$$\tilde{\varepsilon}_{ij} = \tilde{h}_i \tilde{h}_j \varepsilon_{ij} \quad \text{(no sum on } i \text{ and } j\text{)}, \tag{23}$$

and

$$\widetilde{T}^{ij} = \frac{1}{\widetilde{h}_i}\frac{1}{\widetilde{h}_j}T^{ij} \quad \text{(no sum on } i \text{ and } j\text{).} \tag{24}$$

2.4 SPH method

The density ρ in the mathematical space is considered to be equal to that in the physical space, $\widetilde{\rho}$. The mass of a particle in the mathematical space, *m*, is then defined by

$$m = \frac{\widetilde{m}}{\sqrt{g}} = \rho d^3, \tag{25}$$

where *d* is the uniform particle spacing in the initial condition in the mathematical space. Equation (25) indicates that *m* is independent of the scale parameters *a*, *b*, and *c*.

SPH is based on interpolation theory. The method allows a function to be expressed in terms of its values at a set of disordered points using a kernel function. The kernel function *W* refers to a weighting function and specifies the contribution of a field variable $\phi(\mathbf{x})$ at a certain position **x**. The interpolation of $\phi(\mathbf{x})$ is defined as

$$\phi(\mathbf{x}) = \int_D \phi(\mathbf{x}')W(\mathbf{x}-\mathbf{x}', h)\mathrm{d}\mathbf{x}'. \tag{26}$$

D is the volume considered, and the smoothing length *h* represents the effective width of the kernel. The very basic interpolation equation (Eq. (26)) can be evaluated only in mathematical space, since $\mathrm{d}\mathbf{x}' \approx m/\rho = d^3$ is independent of the scale. If there are *N* particles in the effective width of the kernel function from position **x**, Eq. (26) is approximated by

$$\langle \phi(\mathbf{x}) \rangle = \sum_{b=1}^{N} \phi_b \frac{m_b}{\rho_b} W(\mathbf{x}-\mathbf{x}_b, h), \tag{27}$$

where *b* denotes the label of a neighboring particle, and the brackets $\langle \; \rangle$ indicate that the variable is approximated by the SPH interpolation. A particle equation for the gradient of $\phi(\mathbf{x})$ can be obtained by using the divergence theorem of Gauss and the fact that *W* vanishes at infinity.

$$\langle \nabla \phi(\mathbf{x}) \rangle = \int_D \phi(\mathbf{x}') \nabla W(\mathbf{x}-\mathbf{x}', h) \mathrm{d}\mathbf{x}' = \sum_{b=1}^{N} \phi_b \frac{m_b}{\rho_b} \nabla W(\mathbf{x}-\mathbf{x}_b, h) \tag{28}$$

The kernel function should have a symmetric shape that satisfies both the limit condition and the normalization condition. Compact support kernels are usually used for calculation efficiency. A cubic B-spline function is used in this study:

$$W(\mathbf{r}, h) = W_0 \times \begin{cases} 1 - \frac{3}{2}s^2 + \frac{3}{4}s^3 & \text{for } 0 \le s < 1, \\ \frac{1}{4}(2-s)^3 & \text{for } 1 \le s < 2, \\ 0 & \text{otherwise,} \end{cases} \tag{29}$$

where $s = |\mathbf{r}|/h$; the normalization constant W_0 is $10/(7\pi h^2)$ in a two-dimensional analysis, and $1/(\pi h^3)$ in a three-dimensional analysis.

The total time derivative (d/dt) is taken in a moving Lagrangian frame, and the transform of governing equations (13) and (14) into particle equations yields the following set of SPH equations:

$$\frac{\mathrm{d}\rho_a}{\mathrm{d}t} = \rho_a \sum_{b \ne a} \frac{m_b}{\rho_b} \left\{ \left(v^i\right)_a - \left(v^i\right)_b \right\} \frac{\partial W_{ab}}{\partial \theta^i}, \tag{30}$$

$$\frac{\mathrm{d}\left(v^j\right)_a}{\mathrm{d}t} = \sum_{b \ne a} m_b \left\{ \frac{\left(\sigma^{ij}\right)_a}{\rho_a^{\,2}} + \frac{\left(\sigma^{ij}\right)_b}{\rho_b^{\,2}} + \delta^{ij} \tilde{\Pi}_{ab} \right\} \frac{\partial W_{ab}}{\partial \theta^i}, \tag{31}$$

where subscripts a and b denote the labels of the particle of interest and its neighboring particles. $\tilde{\Pi}$ is the artificial viscosity term to stabilize dynamic response and is evaluated in the physical space. Note that δ^{ij} is the tensor converted from the unit tensor in the physical space, $\tilde{\delta}^{ij}$, by the same manner as in Eq. (24). The deformation rate tensor and the spin tensor represented as

$$D_{ij} = \frac{1}{2}\left(v_i\big|_j + v_j\big|_i \right) = \frac{1}{2}\left(\frac{\partial v_i}{\partial \theta^j} + \frac{\partial v_j}{\partial \theta^i} \right) \tag{32}$$

$$W_{ij} = \frac{1}{2}\left(v_i\big|_j - v_j\big|_i \right) = \frac{1}{2}\left(\frac{\partial v_i}{\partial \theta^j} - \frac{\partial v_j}{\partial \theta^i} \right) \tag{33}$$

are discretized by particles in the same manner as with standard SPH.

$$\left(D_{ij}\right)_a = \frac{1}{2}\sum_{a \neq b}\frac{m_b}{\rho_b}\left[\left\{\left(v_i\right)_b - \left(v_i\right)_a\right\}\frac{\partial W_{ab}}{\partial \theta^j} + \left\{\left(v_j\right)_b - \left(v_j\right)_a\right\}\frac{\partial W_{ab}}{\partial \theta^i}\right] \tag{34}$$

$$\left(W_{ij}\right)_a = \frac{1}{2}\sum_{a \neq b}\frac{m_b}{\rho_b}\left[\left\{\left(v_i\right)_b - \left(v_i\right)_a\right\}\frac{\partial W_{ab}}{\partial \theta^j} - \left\{\left(v_j\right)_b - \left(v_j\right)_a\right\}\frac{\partial W_{ab}}{\partial \theta^i}\right] \tag{35}$$

Since all of the variables are written in mathematical space, the same calculation procedure as for standard SPH is available for the above formulation paying attention to the “covariant” (subscript) or “contravariant” (superscript).

2.5 Time integration

The time-step size should be sufficiently small to stably analyze the time integration. Time step Δt is determined by the Courant-Friedrichs-Levy condition.

$$\Delta t = \min\left(\frac{\omega h \times \min[a, b, c]}{\tilde{c} + |\tilde{\mathbf{v}}|}\right) \tag{36}$$

ω is 0.3 to ensure that a particle moves only a fraction of the smoothing length h per time-step. The Runge-Kutta-Gill method was employed as the time-integration scheme.

2.6 Stress boundary condition

For simplicity, the stress boundary condition is expressed by imposing equivalent external forces on the particles in a surface instead of enforcing tractions on the surface. If a body force **F** is given to a particle, the acceleration **F**/ρ is added to the right-hand-side of Eq. (31) for the particle concerned based on the conservation of momentum. If a force $\overline{\mathbf{F}}$ is given to a particle, the corresponding acceleration is first calculated in the physical space.

$$\frac{\mathrm{d}\,\mathbf{v}}{\mathrm{d}\,t} = \frac{\overline{\mathbf{F}}}{\tilde{m}} \tag{37}$$

The acceleration is then converted into that in mathematical space by using Eq. (11) and is added to the acceleration calculated by Eq. (31).

3. Verification

Before applying the proposed approach to specific problems, we first confirmed that valid stresses and strains are predicted for quasi-static uniaxial tension and pure shear. This section verifies the proposed approach by predicting quasi-static three-point bending in a thin plate. Figure 1 depicts the quarter model for three-point bending, considering the symmetry. The model was 40 mm long, 5 mm wide, and 2 mm thick. Particles were arranged with regular spacing in the generalized coordinate system (Fig. 1c). It should be noted that the aspect ratio of the whole plate was altered after mapping. The total number of particles was varied depending on the scale parameters, and were calculated by (length / a) × (width / b) × (thickness / c) in this analysis. An external force in the $-z$ ($+z$) direction was given to each particle in the left (right) yz-plane at the center of the thickness. The absolute value of the external force at each particle increased linearly at the rate of 0.05 N/ms until 1 ms, and was then kept constant till the end of the analysis (2 ms). The sum of the external forces at the left or right yz-plane was 0.5 N after 1 ms. The material was assumed to be isotropic, and the material properties listed in Table 1 were used.

Figure 2 depicts the distribution of the bending stress $\tilde{\sigma}_{11}$ ($=\sigma_x$) at 1 ms in the model with a=0.2, b=1, and c=0.1. A compressive (tensile) stress was observed on the upper (lower) surface, and the absolute value of the bending stress decreased to zero at the support point ($x = x_{max}$). Stresses were calculated by SPH interpolation, and their absolute value at particles near a surface was always less than the exact solution, because they had an insufficient number of neighboring particles for Eq. (27).

The accuracy was investigated for scale parameters a and c. The deflection $\Delta z(x)$ of three-point bending is derived from the classical beam theory as follows, where the deflection at the loading point (x=0) is considered to be zero.

$$\Delta z(x)=\frac{P}{6EI}\left(3L^2x-x^3\right) \tag{38}$$

P is the concentrated load, E is the Young's modulus, I is the second moment of area, and L is the half length of the beam, which was equal to the model length in Fig. 1. Assuming that the predicted deflection was represented by a cubic function of x, the apparent coefficient $P/(6EI)$ was estimated by minimizing the error sum of squares between the predicted deflection and the theory by Eq. (38). Figure 3 plots the estimated coefficient $P/(6EI)$ against scale parameters a and c. The coefficient decreased with increasing parameter a (decreasing the number of divisions in the longitudinal direction), but within the range investigated, the parameter c (the number of divisions in the through-thickness direction) had little effect on the deformation state. A smaller parameter a provided a saturated value near the exact solution (3.37×10^{-7} mm^{-2}), whereas a too large parameter a resulted in a large error in the coefficient $P/(6EI)$ because of a incorrect stress distribution near the supporting point.

The bending stress $\tilde{\sigma}_{11}(z)$ in the beam theory is represented by

$$\tilde{\sigma}_{11}(z)=-\frac{M}{I}z, \tag{39}$$

where M is the bending moment at position x. The apparent coefficient M/I was estimated for a set of parameters a and c by approximating the predicted bending stress distribution by a linear function of z. Figure 4 plots the coefficient M/I against parameters a and c, where the stress $\tilde{\sigma}_{11}$ on a line (x,y) = (x_{min},y_{min}) was used for evaluation. A small parameter a provided a stress distribution that almost coincided with the exact solution (M/I = 6.0 N·mm^{-3}), but the parameter c had little effect on the slope of the bending stress, as is the case with the deflection (Fig. 3).

The accuracy of the present approach was compared with standard SPH with an insufficient number of particles to clarify its advantage. The model was the same as in Fig. 1 except for the width (4 mm). The loading pattern was also the same as in the preceding analysis, and the sum of the external forces was adjusted to 0.4 N. The spacing between two particles was 0.4 mm in standard SPH, and there were 5000 particles. The spacing in the present approach was set to 0.4 mm in the x-direction, 1.33 mm in the y-direction, and 0.125 mm in the z-direction by setting the scale parameters to a=0.4, b=1.33, and c=0.125. There was a total of 4800 particles, which was less than in the conventional model. Figure 5a compares the deflection between the two predictions and the theory. The standard SPH exhibited a considerable error because of the insufficient number of particles in the through-thickness direction, but the present approach agreed with the theory despite the smaller number of particles. Figure 5b plots the bending stress on a line $(x,y) = (x_{min},y_{min})$. The absolute value of the slope (M/I) of the present approach (M/I = 5.96) almost coincided with that of the theory (M/I = 6.0), but that of the conventional model (M/I = 1.57) was much smaller than the theoretical value. Moreover, the present approach provided more accurate maximum bending stress than the conventional model. The present approach thus enabled us to employ fine division only in the required direction and to improve the accuracy without increasing the calculation cost.

4. High-velocity impact

High-velocity impact is analyzed by the improved SPH as a dynamic case, and predictions are compared with experiment results. This section first summarizes the experiment and then discusses the validity and advantage of SPH in a generalized coordinate system.

4.1 Experiment

High-velocity impact tests were performed using a gas gun. The target plate was made of 5052 aluminum alloy, and the projectile was made of bearing steel. The target plate was 165 mm long, 50 mm wide, and 3 mm thick; the projectile sphere had a diameter of 6 mm. Figure 6 depicts the schematic of the experiment setup. Twenty-five millimeters of the target was clamped into a jig, and the impact point was the center of the remaining part. The projectile was loaded in a sabot, which was made of expanded polystyrene foam, and was accelerated by compressed air. The sabot was stopped at the mouth of the gun, and inertia carried the projectile forward. The impact velocity was calculated by measuring the time to pass a given path (500 mm) using lasers and photodetectors.

Figure 7a presents an overview of the target specimen impacted at 135 m/s. A crater was generated at the impact point, but large permanent deformation was observed only in a limited area. The three-dimensional shape of the impacted target was specified by a noncontact 3D-digitizer (RANGE7, Konica Minolta). Figures 7b and 7c present the measured shapes of the front and the back surfaces near the impact point. The depth of the crater was 1.20 mm, and the distance between the front surface and the top of the bump on the back surface was 3.81 mm.

4.2 Analysis

We analyzed the impact problem with three sets of scale parameters $(a,b,c) = (1,1,1)$ (i.e., standard SPH), (1.5,1.5,1), and (2,2,1). A typical analytical model is depicted in Fig. 8. Only quarter of the specimen was modeled considering symmetry, and the target plate was 12 mm long, 12 mm wide, and 3 mm thick; the projectile diameter was 6 mm. The initial distance between two adjacent particles was 0.125 mm at a scale parameter of unity, and the total number of particles was 235648, 104778 and 58906 for the cases $(a,b,c) = (1,1,1)$, (1.5,1.5,1) and (2,2,1), respectively. The target was not fixed, and the projectile moved at an initial velocity of 135 m/s in the $-x_3$-direction. The material properties are listed in Table 2. A symmetric boundary condition was expressed by temporarily copying neighboring particles just opposite the symmetry plane, and this handling was performed only in the particles whose effective range exceeded that plane. It should be noted that sign inversion was required for some quantities of the temporarily-copied particles.

Figure 9 presents the pressure distribution predicted by the three models. These results agreed well with each other, but the high-pressure region was broadened slightly by a greater scale parameter. The effective radii of the three models were the same in the mathematical space, but in the physical space, the effective ellipsoidal region became larger due to a greater scale parameter. This may be the reason for the marginal discrepancy in the pressure distribution.

Figure 10 compares the deformation of the target between the experiment and the predictions by the three models. The deformation obtained by standard SPH was generally consistent with the measurement. Greater scale parameters also reproduced close crater shapes, but the depth of the crater decreased with increasing scale parameters because the local high stresses were smoothed in the x_1x_2-plane by increasing parameters a and b. There was a difference between the measured final deformed shape and the predicted one. The major cause of this difference will be the constitutive model. The classical elastic-plastic theory can describe the strain hardening effect, but cannot consider effects of strain rate and temperature. A constitutive model including these effects, e.g., Johnson-Cook viscoplastic model, will diminish the difference.

Finally, Fig. 11 presents the computation time versus the number of particles. The computation time decreased as the 1.17th power of the number of particles. Compared with standard SPH, i.e., $(a,b,c) = (1,1,1)$, the present approach with scale parameters of (2,2,1) took only 25% of the number of particles and 17% of the computation time. The characteristics of this approach thus reduced the calculation cost by reducing the number of divisions in a direction with a moderate change in the stress field.

5. Conclusions

This study proposed a numerical scheme of smoothed particle hydrodynamics (SPH) solving in a generalized coordinate system. Particles were first allocated inhomogeneously in the physical Cartesian coordinate system and then were arranged homogeneously in a generalized coordinate system, thanks to the use of scaled base vectors. The governing equations were solved in the generalized coordinate system, but the numerical scheme was the same as with standard SPH. This study verified the present approach by investigating quasi-static three-point bending of a thin plate and applied it to high-velocity impact problems. The conclusions are summarized below.

1. The present approach with an adequate set of scale parameters significantly improved the accuracy in the bending-stress distribution in a thin plate without increasing the calculation cost, compared with standard SPH with an insufficient number of particles. The accuracy in the bending-stress distribution was improved remarkably by employing fine division in the longitudinal and through-thickness directions.
2. The predicted shape of the crater agreed well with the experiment measurement regardless of the scale parameters. Moreover, the pressure distribution obtained by the present approach coincided with that of standard SPH. These results confirmed the numerical scheme of SPH in a generalized coordinate system.
3. The numerical results revealed that the calculation time decreased as the 1.17th power of the number of particles. Unlike standard SPH, fine division occurs only in a required direction, and this characteristic reduced the calculation cost by reducing the number of divisions in a direction with a moderate change in the stress field.

Acknowledgments

S. Y. acknowledges the support of the Japan Society for the Promotion of Science (JSPS) under Grants-in-Aid for Scientific Research (No. 25289306). S. Y. and T. O. also acknowledge the support of the Japan Science and Technology Agency through Cross-ministerial Strategic Innovation Promotion Program (SIP). The authors thank Mr. D. Komagata (Tohoku University) and Mr. T. Ikawa (Shizuoka University) for their great efforts. The authors also express appreciation to Dr. A. Yoshimura (Japan Aerospace Exploration Agency) for his support in the experiment.

References

[1] Gingold RA, Monaghan JJ. Smoothed particle hydrodynamics: theory and application to non-spherical stars. *Monthly Notices of the Royal Astronomical Society* 1977; **181**:375-389.

[2] Lucy LB. A numerical approach to the testing of the fission hypothesis. *Astronomical Journal* 1977; **82**:1013-1024.

[3] Belytschko T, Lu YY, Gu L. Element-free Galerkin methods. *International Journal for Numerical Methods in Engineering* 1994; **37**:229-256.

[4] Liu WK, Jun S, Li S, Adee J, Belytschko T. Reproducing kernel particle methods for structural dynamics. *International Journal for Numerical Methods in Engineering* 1995; **38**:1655-1679.

[5] Atluri SN, Zhu T. A new Meshless Local Petrov-Galerkin (MLPG) approach in computational mechanics. *Computational Mechanics* 1998; **22**:117-127.

[6] Sulsky DL, Kaul A. Implicit dynamics in the material-point method. *Computer Methods in Applied Mechanics and Engineering* 2004; **139**:1137-1170.

[7] Bardenhagen S, Kober E. The generalized interpolation material point method. *Computer Modeling in Engineering & Sciences* 2004; **5**:477-495.

[8] Wallstedt PC, Guilkey JE. A weighted least squares particle-in-cell method for solid mechanics. *International Journal for Numerical Methods in Engineering* 2011; **85**:1687-1704.

[9] Randles PW, Libersky LD. Normalized SPH with stress points. *International Journal for Numerical Methods in Engineering* 2000; **48**:1455-1462.

[10] Sanchez JJ, Randles PW. Dynamic failure simulation of quasi-brittle material in dual particle dynamics. *International Journal for Numerical Methods in Engineering* 2012; **91**:1227-1250.

[11] Li B, Habbal F, Ortiz M. Optimal transportation meshfree approximation schemes for fluid and plastic flows. *International Journal for Numerical Methods in Engineering* 2010; **83**:1541-1579.

[12] Rabczuk T, Gracie R, Song J-H, Belytschko T. Immersed particle method for fluid–structure interaction. *International Journal for Numerical Methods in Engineering* 2010; **81**:48-71.

[13] Nguyen VP, Rabczuk T, Bordas S, Duflot M. Meshless methods: A review and computer implementation aspects. *Mathematics and Computers in Simulation* 2008; **79**:763-813.

[14] Monaghan JJ. Simulating free surface flows with SPH. *Journal of Computational Physics* 1994; **110**: 399-406.

[15] Takeda H, Miyama SM, Sekiya M. Numerical simulation of viscous flow by smoothed particle hydrodynamics. *Progress of Theoretical Physics* 1994; **92**:939-960.

[16] Morris JP, Fox PJ, Zhu Y. Modeling low Reynolds number incompressible flows using SPH. *Journal of Computational Physics* 1997; **136**:214-226.

[17] Lee ES, Moulinec C, Xu R, Violeau D, Laurence D, Stansby P. Comparisons of weakly compressible and truly incompressible algorithms for the SPH mesh free particle method.

Journal of Computational Physics 2008; **227**:8417-8436.

[18] Szewc K, Pozorski J, Minier JP. Analysis of the incompressibility constraint in the smoothed particle hydrodynamics method. *International Journal for Numerical Methods in Engineering* 2012; **92**: 343-369.

[19] Libersky LD, Petschek AG, Carney TC, Hipp JR, Allahdadi FA. High strain Lagrangian hydrodynamics: a three-dimensional SPH code for dynamic material response. *Journal of Computational Physics* 1993; **109**:67-75.

[20] Benz W, Asphaug E. Simulations of brittle solids using smooth particle hydrodynamics. Computer Physics Communications 1995; **87**:253-265.

[21] Johnson GR, Stryk RA, Beissel SR. SPH for high velocity impact computations. *Computer Methods in Applied Mechanics and Engineering* 1996; **139**:347-373.

[22] Randles PW, Libersky LD. Smoothed particle hydrodynamics: some recent improvements and applications. *Computer Methods in Applied Mechanics and Engineering* 1996; **139**:375-408.

[23] Gray JP, Monaghan JJ, Swift RP. SPH elastic dynamics. *Computer Methods in Applied Mechanics and Engineering* 2001; **190**:6641-6662.

[24] Antoci C, Gallati M, Sibilla S. Numerical simulation of fluid-structure interaction by SPH. *Computers & Structures* 2007; **85**:879-890.

[25] Rafiee A, Thiagarajan KP. An SPH projection method for simulating fluid-hypoelastic structure interaction. *Computer Methods in Applied Mechanics and Engineering* 2009; **198**:2785-2795.

[26] Lee M, Yoo YH. Analysis of ceramic/metal armour systems. *International Journal of Impact Engineering* 2001; **25**:819-829.

[27] Shintate K, Sekine H. Numerical simulation of hypervelocity impacts of a projectile on

laminated composite plate targets by means of improved SPH method. *Composites Part A* 2004; **35**:683-692.

[28] Michel Y, Chevalier JM, Durin C, Espinosa C, Malaise F, Barrau JJ. Hypervelocity impacts on thin brittle targets: Experimental data and SPH simulations. *International Journal of Impact Engineering* 2006; **33**:441-451.

[29] Takaffoli M, Papini M. Material deformation and removal due to single particle impacts on ductile materials using smoothed particle hydrodynamics. *Wear* 2012; **274-275**:50-59.

[30] Cleary PW, Ha J, Prakash M, Nguyen T. 3D SPH flow predictions and validation for high pressure die casting of automotive components. *Applied Mathematical Modelling* 2006; **30**:1406-1427.

[31] Cleary PW, Prakash M, Das R, Ha J. Modelling of metal forging using SPH. *Applied Mathematical Modelling* 2012; **36**:3836-3855.

[32] Lee ES, Violeau D, Issa R, Ploix S. Application of weakly compressible and truly incompressible SPH to 3-D water collapse in waterworks. *Journal of Hydraulic Research* 2010; **48**:50-60.

[33] Gray JP, Monaghan JJ. Numerical modelling of stress fields and fracture around magma chambers. *Journal of Volcanology and Geothermal Research* 2004; **135**:259-283.

[34] Prakash M, Cleary PW, Three dimensional modelling of lava flow using smoothed particle hydrodynamics. *Applied Mathematical Modelling* 2011; **35**:3021-3035.

[35] Monaghan JJ. Smoothed particle hydrodynamics. *Reports on Progress in Physics* 2005; **68**:1703-1759.

[36] Liu MB, Liu GR. Smoothed particle hydrodynamics (SPH): an overview and recent developments. *Archives of Computational Methods in Engineering* 2010; **17**:25-76.

[37] Wong S, Shie Y. Galerkin based smoothed particle hydrodynamics. *Computers &*

Structures 2009; 87:1111-1118.

[38] Herreros MI, Mabssout M. A two-steps time discretization scheme using the SPH method for shock wave propagation. *Computer Methods in Applied Mechanics and Engineering* 2011; **200**:1833-1845.

[39] Blanc T, Pastor M. A stabilized Runge–Kutta, Taylor smoothed particle hydrodynamics algorithm for large deformation problems in dynamics. *International Journal for Numerical Methods in Engineering* 2012; **91**:1427-1458.

[40] Colagrossi A, Bouscasse B, Antuono M, Marronea S. Particle packing algorithm for SPH schemes. *Computer Physics Communications* 2012; **183**:1641-1653.

[41] Vacondio R, Rogers BD, Stansby PK, Mignosa P, Feldman J. Variable resolution for SPH: A dynamic particle coalescing and splitting scheme. *Computer Methods in Applied Mechanics and Engineering* 2013; **256**:132-148.

[42] Puri K, Ramachandran P. A comparison of SPH schemes for the compressible Euler equations. *Journal of Computational Physics* 2014; **256**:308-333.

[43] Maurel B, Combescure A. An SPH shell formulation for plasticity and fracture analysis in explicit dynamics. *International Journal for Numerical Methods in Engineering* 2008; **76**:949-971.

[44] Caleyron F, Combescure A, Faucher V, Potapov S. Dynamic simulation of damage-fracture transition in smoothed particles hydrodynamics shells. *International Journal for Numerical Methods in Engineering* 2012; **90**:707-738.

[45] Yashiro S, Ogi K, Yoshimura A, Sakaida Y. Characterization of high-velocity impact damage in CFRP laminates: Part II – prediction by smoothed particle hydrodynamics. *Composites Part A* 2014; **56**:308-318.

Table 1 Material properties used in three-point bending.

Density (kg/m^3)	2.785×10^3
Bulk sound speed (m/s)	5.328×10^3
Shear modulus (GPa)	27.6
Young’s modulus (GPa)	74.2
Poisson’s ratio	0.344

Table 2 Material properties used in high-velocity impact.

	Aluminum plate	Steel projectile
Density (kg/m^3)	2.68×10^3	7.83×10^3
Bulk sound speed (m/s)	5.06×10^3	4.73×10^3
Shear modulus (GPa)	26.3	80.8
Initial yield stress (MPa)	214	1648
Hardening coefficient H'	1.24×10^3	66.5×10^3

Figure captions

Fig. 1 Analytical model for three-point bending of a thin plate with $a = 0.2$, $b = 1$, and $c = 0.1$, considering the symmetry.

Fig. 2 Contour plot of the bending stress $\tilde{\sigma}_{11}$ at 1 ms with $a = 0.2$, $b = 1$, and $c = 0.1$.

Fig. 3 Change in the apparent coefficient $P/(6EI)$ for representing the deflection against scale parameters a and c.

Fig. 4 Change in the apparent coefficient M/I for representing the bending stress against scale parameters a and c. The stress at $(x,y) = (x_{min},y_{min})$ was used for evaluation.

Fig. 5 Comparison of (a) deflection and (b) bending stress between the present approach and the standard model.

Fig. 6 Schematic of the experiment setup for the high-velocity impact test.

Fig. 7 Deformation of the impacted target plate.

Fig. 8 Typical analytical model for high-velocity impact with $a = 2$, $b = 2$, and $c = 1$, considering the symmetry.

Fig. 9 Snapshots of the pressure distribution after contact: (a) 0 μs, (b) 4 μs, (c) 8 μs, (d) 12 μs, and (e) 16 μs.

Fig. 10 Comparison of the crater shape between the experiment and the predictions. The predictions in the range within $x>0$ ($x<0$) are the surface shapes of the *xz*- (*yz*-) plane.

Fig. 11 Computation time versus number of particles.

Table caption

Table 1 Material properties used in three-point bending.

Table 2 Material properties used in high-velocity impact.

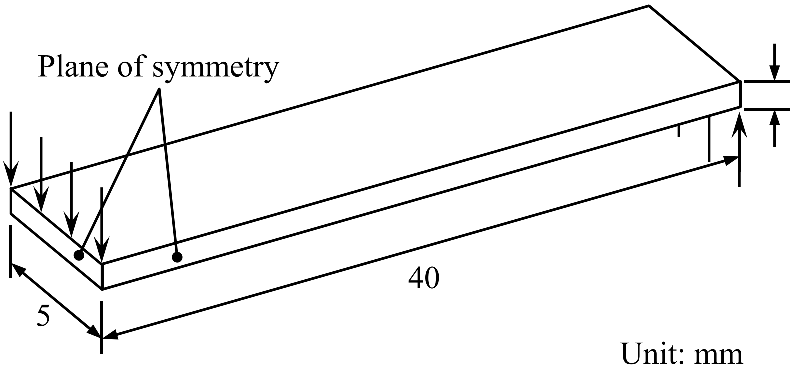

(a) Schematic

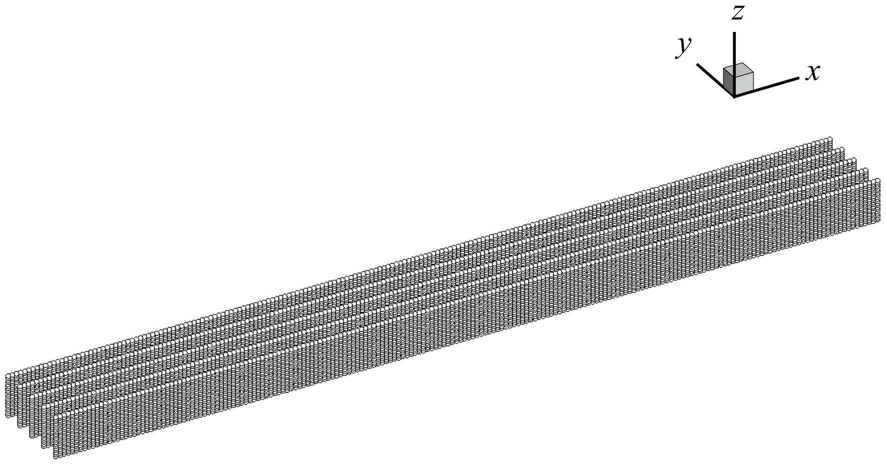

(b) Particle-model in the physical space

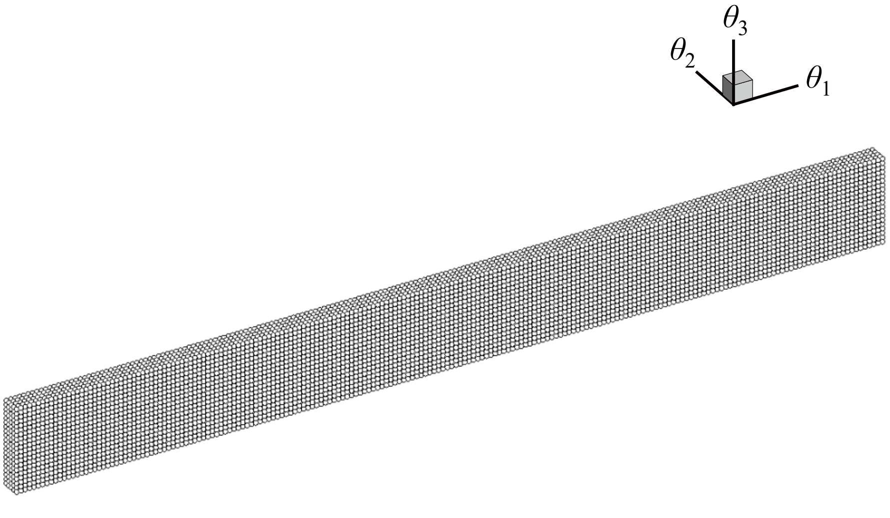

(c) Particle-model in the mathematical space

Fig. 1 Analytical model for three-point bending of a thin plate with $a = 0.2$, $b = 1$, and $c = 0.1$, considering the symmetry.

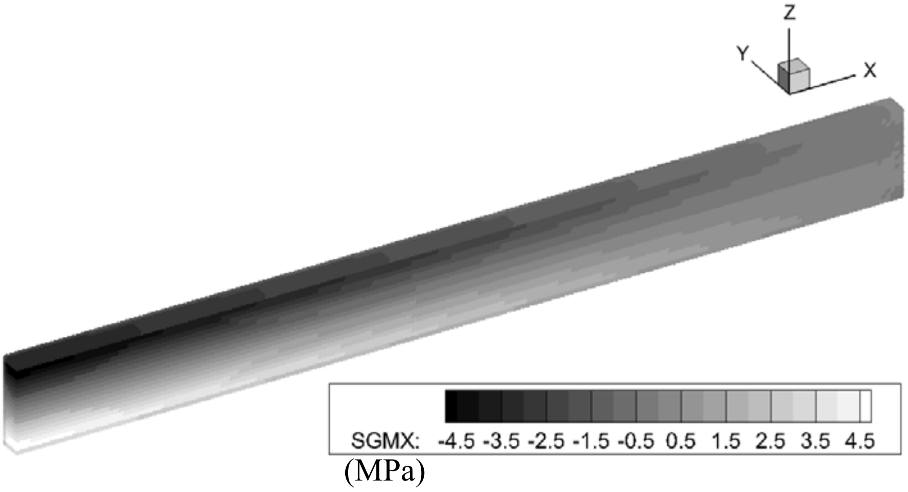

Fig. 2 Contour plot of the bending stress $\widetilde{\sigma}_{11}$ at 1 ms with $a = 0.2$, $b = 1$, and $c = 0.1$.

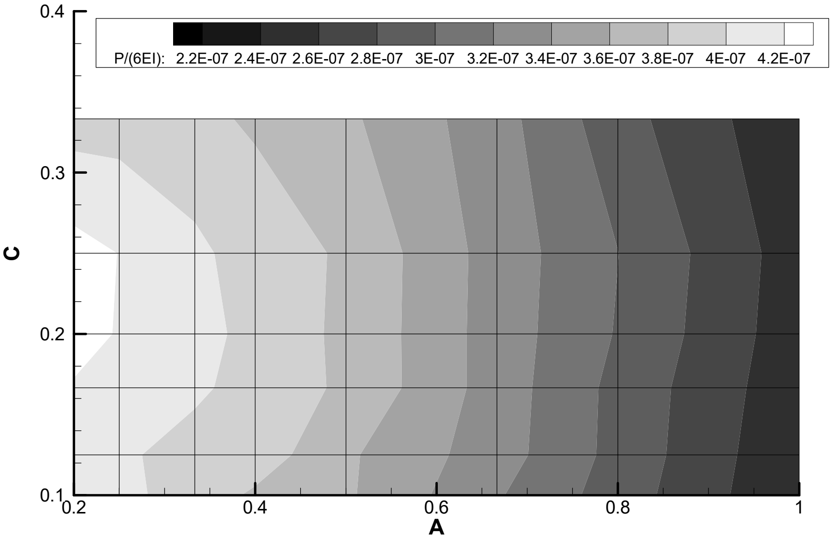

(a) Contour map

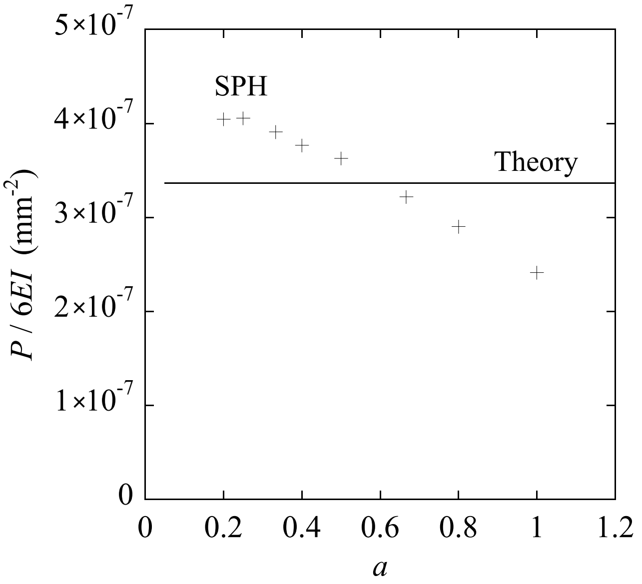

(b) Division in the longitudinal (x) direction ($c = 0.1$)

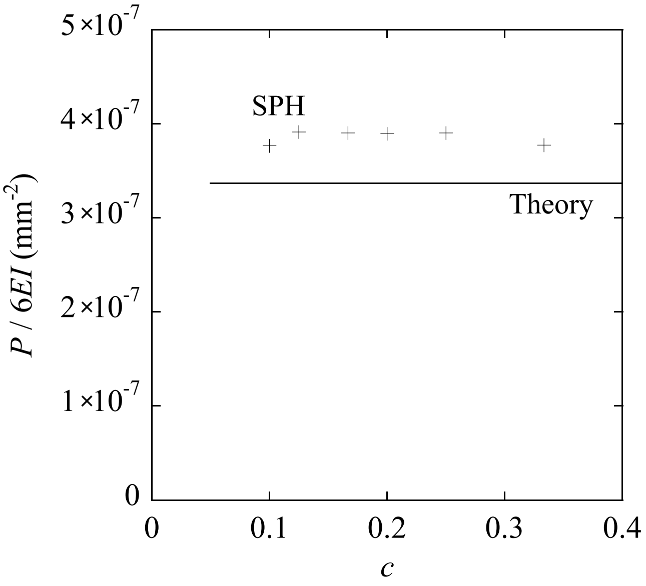

(c) Division in the through-thickness (z) direction ($a = 0.4$)

Fig. 3 Change in the apparent coefficient $P/(6EI)$ for representing the deflection against scale parameters a and c.

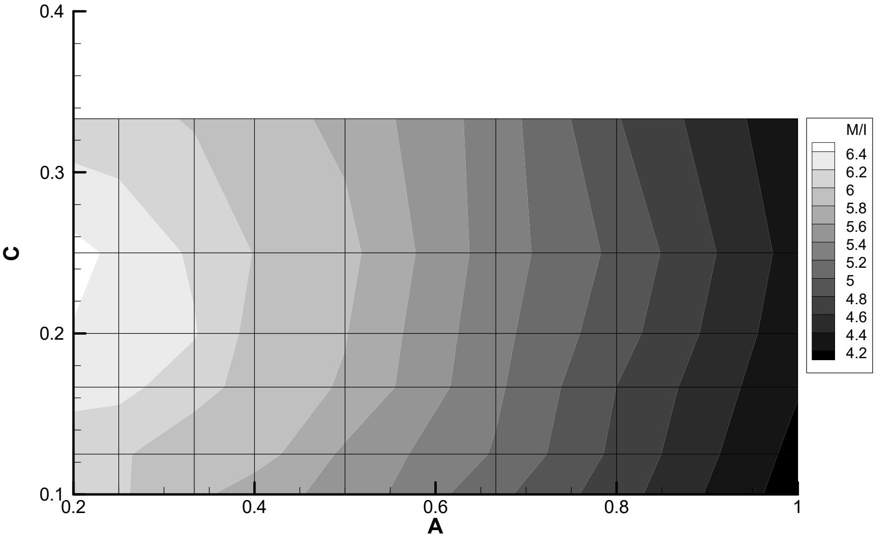

(a) Contour map

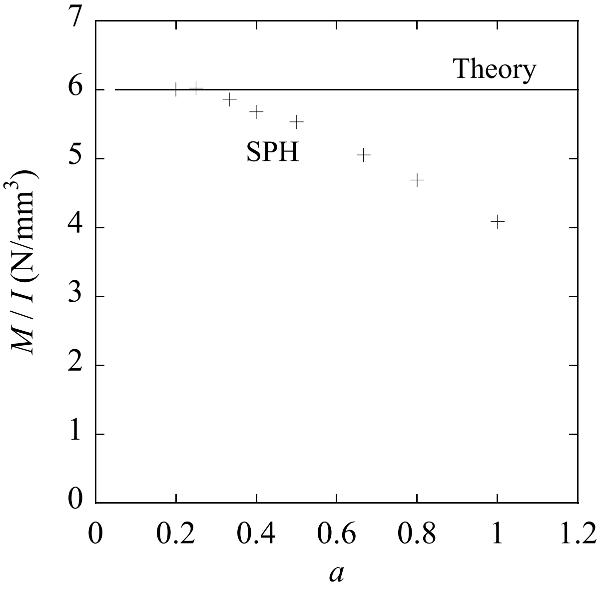

(b) Division in the longitudinal (*x*) direction (*c* = 0.1)

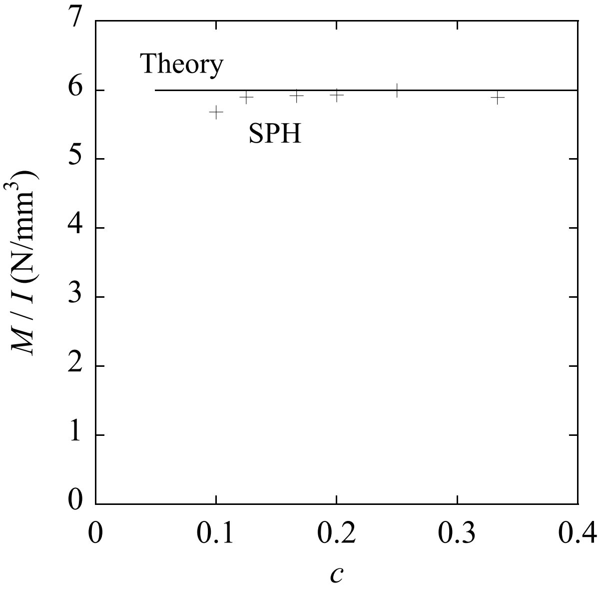

(c) Division in the through-thickness (*z*) direction (*a* = 0.4)

Fig. 4 Change in the apparent coefficient M/I for representing the bending stress against scale parameters a and c. The stress at $(x,y) = (x_{min},y_{min})$ was used for evaluation.

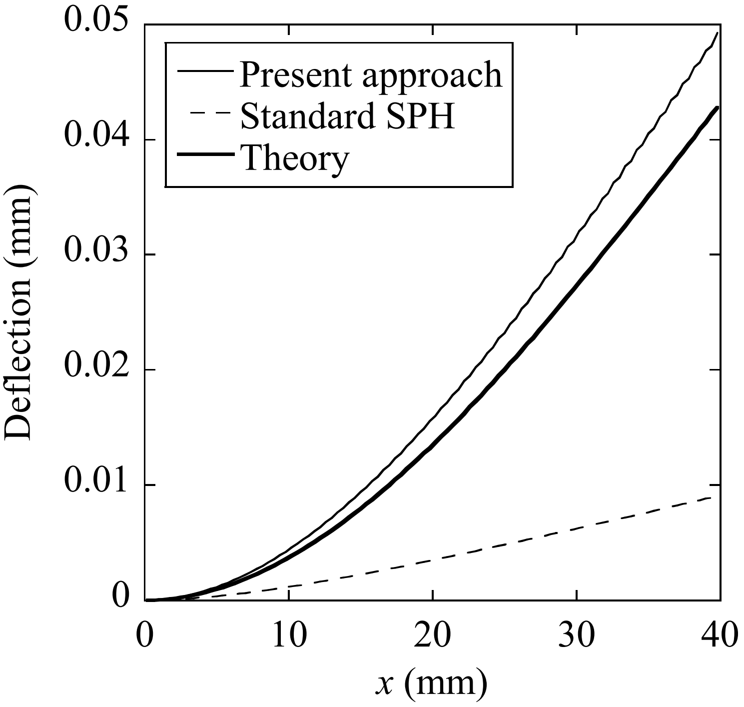

(a) Deflection

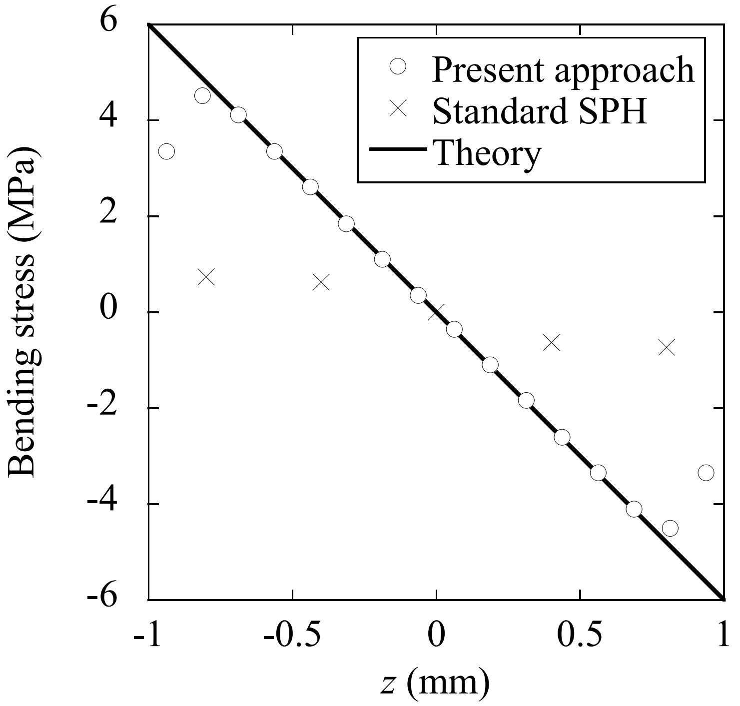

(b) Bending stress

Fig. 5 Comparison of (a) deflection and (b) bending stress between the present approach and the standard model.

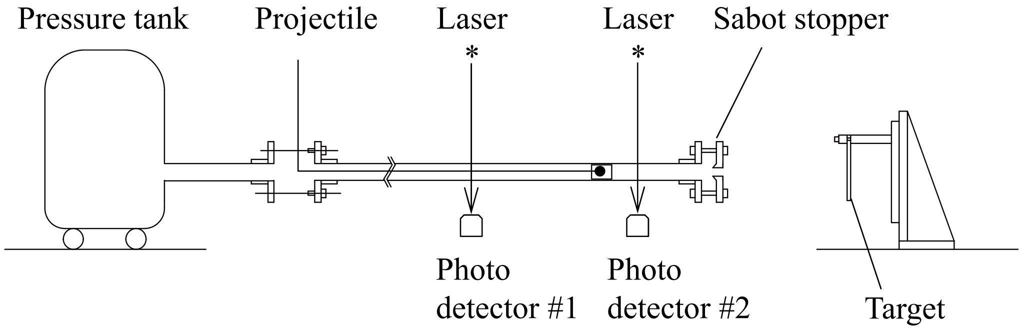

Fig. 6 Schematic of the experiment setup for the high-velocity impact test

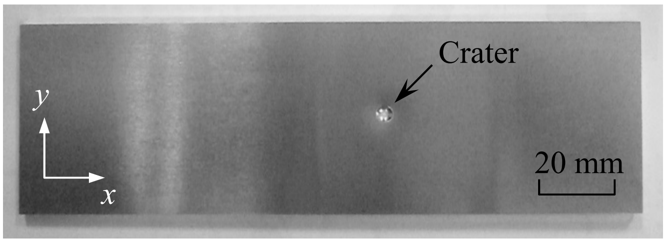

(a) Overview

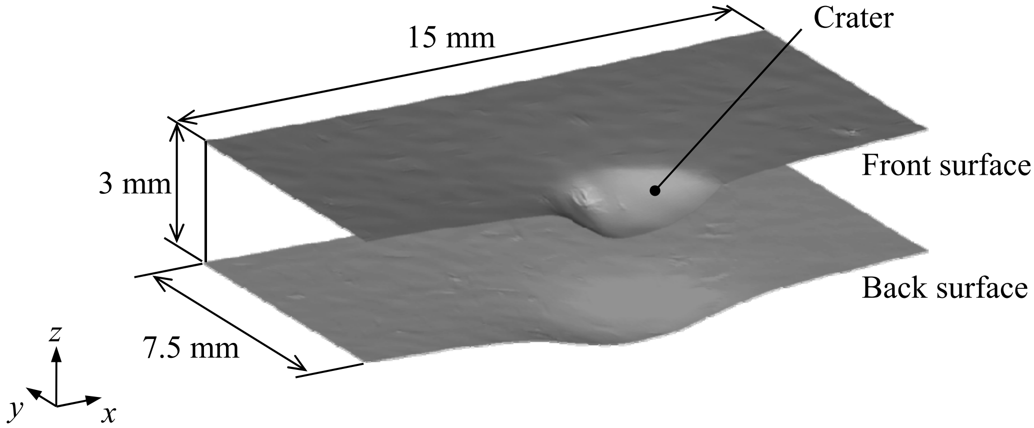

(b) Three-dimensional view

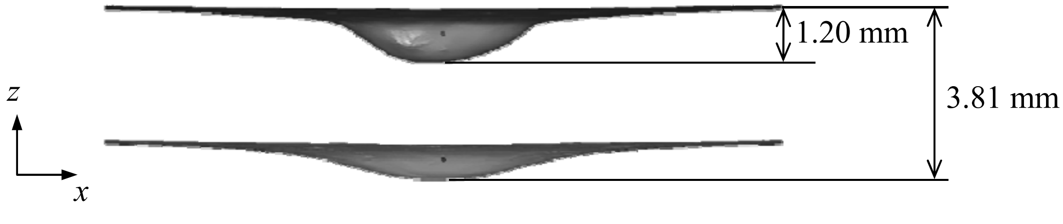

(c) *x*-*z* projection view

Fig. 7 Deformation of the impacted target plate.

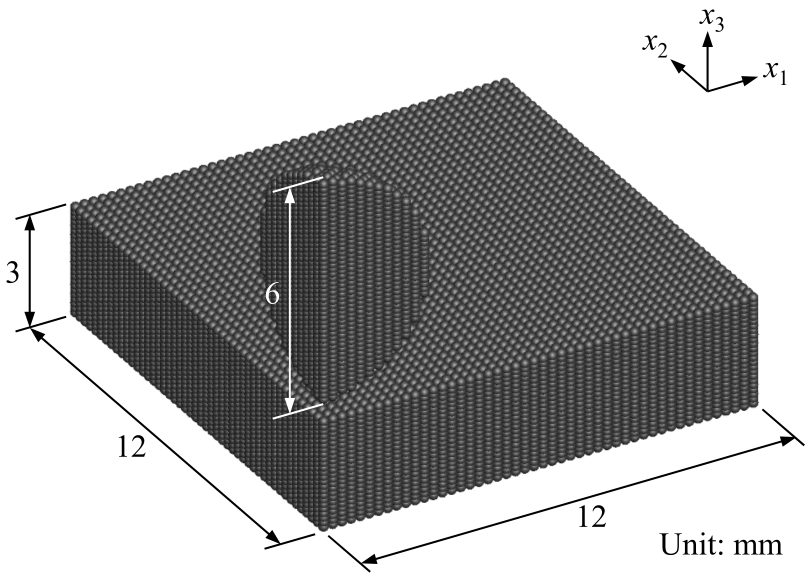

(a) Physical space

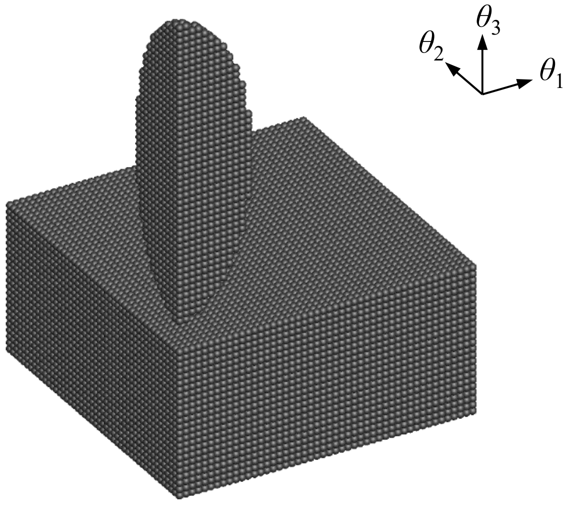

(b) Mathematical space

Fig. 8 Typical analytical model for high-velocity impact with a=2, b=2, and c=1, considering the symmetry.

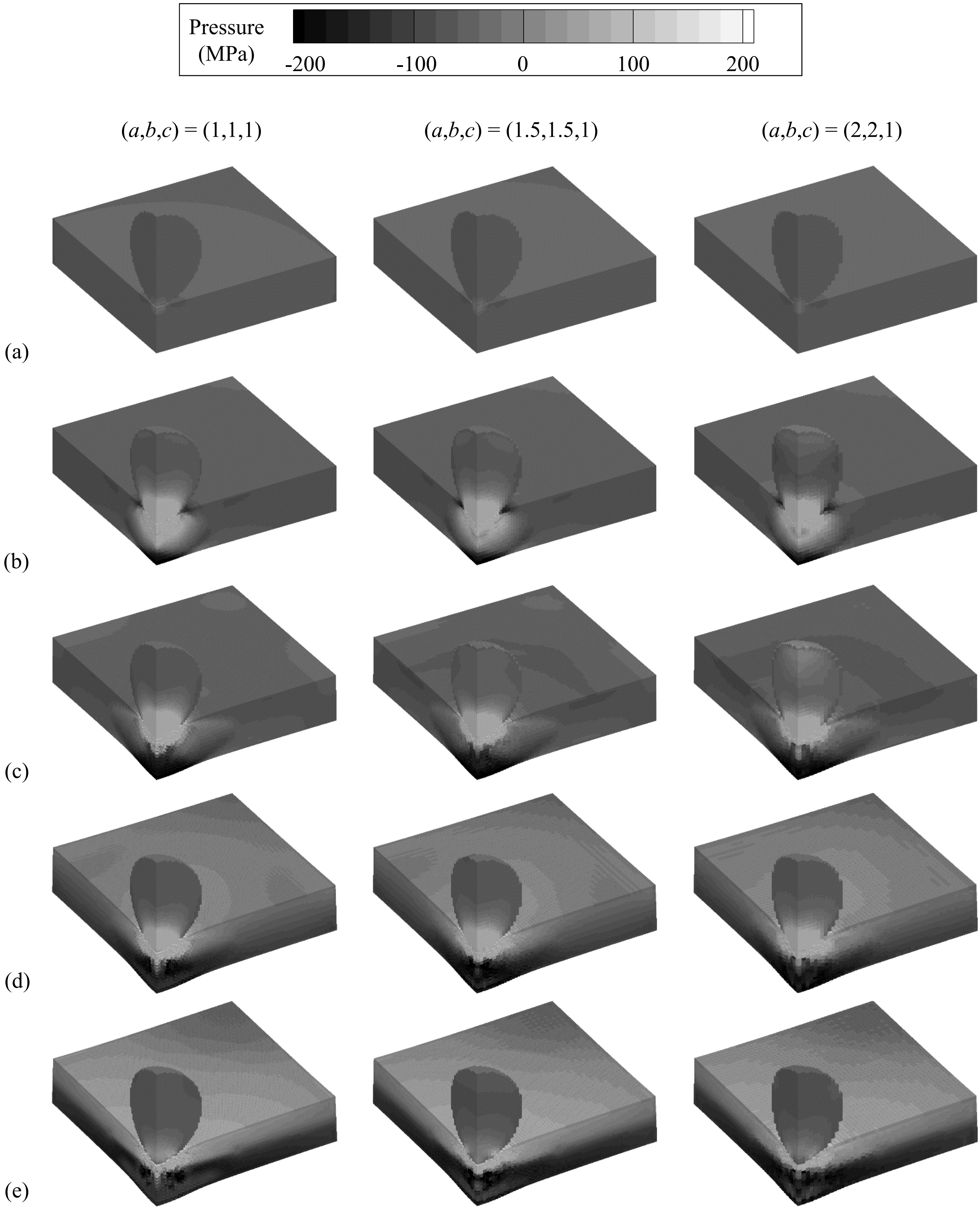

Fig. 9 Snapshots of the pressure distribution after contact: (a) 0 μs, (b) 4 μs, (c) 8 μs, (d) 12 μs, and (e) 16 μs.

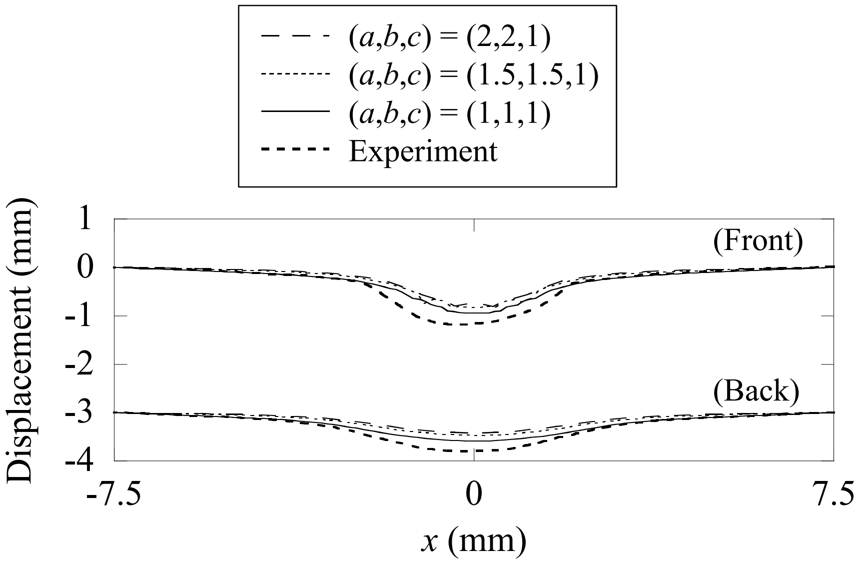

Fig. 10 Comparison of the crater shape between the experiment and the predictions. The predictions in the range within $x > 0$ ($x < 0$) are the surface shapes of the *xz*- (*yz*-) plane.

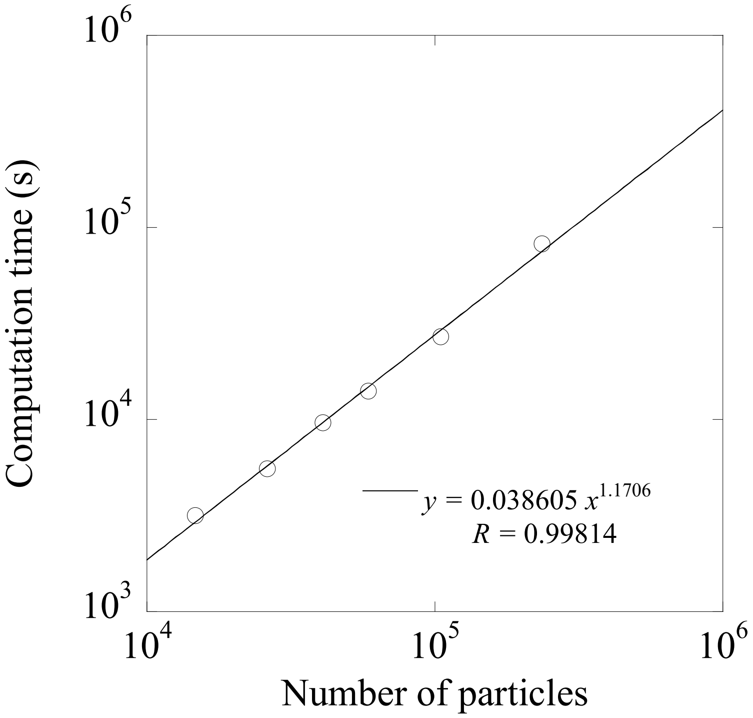

Fig. 11 Computation time versus number of particles.